*Meteoritics & Planetary Science* 38, Nr 8, 1263–1281 (2003)
Abstract available online at http://meteoritics.org

# Partitioning of Ca and Al between forsterite and silicate melt in dynamic systems with implications for the origin of Ca, Al-rich forsterites in primitive meteorites

Andreas PACK[1, 2*] and Herbert PALME[1]

[1]Institute of Mineralogy and Geochemistry, Zülpicher Strasse 49b, 50674 Köln, Germany
[2]CNRS Centre de Recherches Pétrographiques et Géochimiques, 15 rue Notre Dame des Pauvres, 54501 Vandoeuvre lès Nancy, France
*Corresponding author. E-mail: apack@crpg.cnrs-nancy.fr

*(Received 2 December 2002; revision accepted 4 August 2003)*

**Abstract–**We report the results of dynamic crystallization experiments that were specifically designed to study the dependence of Ca and Al partitioning between forsterite and melt in rapidly cooling Ca- and Al-rich melts. The partitioning of Ca between olivine and silicate melt is found to be independent of the cooling rate within the range of 1.5 to 1000°C/hr and at CaO contents of up to 25 wt%. Within analytical uncertainty, our data plot on the equilibrium partitioning curve obtained by Libourel (1999). The partitioning behavior of Al at high cooling rates is more complex. Aluminum is much more heterogenously distributed in the olivine and the co-existing melt than Ca. But, no systematic trend of Al partition coefficient with cooling rate is observed. We apply the results of the experiments to the formation of meteoritic forsterites with relatively high contents of Ca and Al. Although these forsterites are found frequently inside chondrules, the Ca contents of their host chondrules are far too low to crystallize these high Ca-forsterites. This is also true for very rapid cooling of chondrule melts. The parental melt of these forsterites requires CaO contents above 20 wt%.

## INTRODUCTION

### Refractory Forsterites

#### *Characteristics of Refractory Forsterites*

Unequilibrated chondrites contain a population of forsterites that are extremely poor in FeO (0.2–1 mol% fa), Mn (30–40 ppm), and Ni (1–2 ppm) and rich in refractory lithophile elements, such as Ca, Al, Ti, Sc, V, and REE (see Weinbruch et al. 2000; Klerner et al. 2000). These forsterites are termed "refractory forsterites" (RF). They contain up to 0.8 wt% CaO, 0.2–0.3 wt% $Al_2O_3$, and up to 1000 ppm $TiO_2$. RFs occur as isolated grains within the matrices of carbonaceous chondrites (see Fig. 1) and within chondrules, therein mostly as relicts (e.g., Jones 1992, 1996). RFs can be identified by their cathodoluminescence (CL; see Fig. 1b), which distinguishes them from more ferrous olivines (e.g., Steele 1985, 1986; Pack et al. 2002b).

The refractory core of forsterite grain RF03 from Allende (Fig. 1) contains 0.5 wt% FeO, 0.67 wt% CaO, 0.21 wt% $Al_2O_3$, and 0.05 wt% $TiO_2$, a composition typical of RF. The CaO and $Al_2O_3$ contents decrease toward the rim to 0.1 and <0.02 wt%, respectively, while FeO increases to ~30 wt%.

A further characteristic of RFs is that they often show excesses in $^{16}O$ of up to 10 per mil ($\Delta^{17}O = -10‰$; Hervig and Steele 1992; Weinbruch et al. 1993; Leshin et al. 1997; Saxton et al. 1998; Sears et al. 1998; Jones et al. 2000). The degree of $^{16}O$-enrichment is decoupled from the O-isotopic composition of the host meteorite. That the abundance of RF is very similar in unequilibrated ordinary and carbonaceous chondrites is notable, although carbonaceous chondrites contain much more refractory components, such as Ca, Al-rich inclusions (Pack and Palme 2001). Also, the abundance of refractory forsterite is not related to the oxidation state of the host meteorite. This points to the formation of RF from a common, single reservoir or at least by similar processes, independent of the history of the main fraction of the meteorite.

#### *Origin of RF*

The origin of RF is discussed within the framework of 2 end member models. Weinbruch et al. (2000) suggest that RF formed by condensation from the solar nebula. A nebular origin is supported by the extremely low Fe, Mn, and Ni contents (Palme and Fegley 1990; Weinbruch et al. 2000) and by the enrichment in $^{16}O$.

Most authors, however, believe that RF crystallized from FeO-poor type-I chondrules (McSween 1977; Roedder 1981; Jones 1992, 1996). Using the typical CaO concentrations of RF of 0.6–0.8 wt% and the Ca partitioning data by Libourel (1999), the parent melts of RF must have


© Meteoritical Society, 2003. Printed in USA.

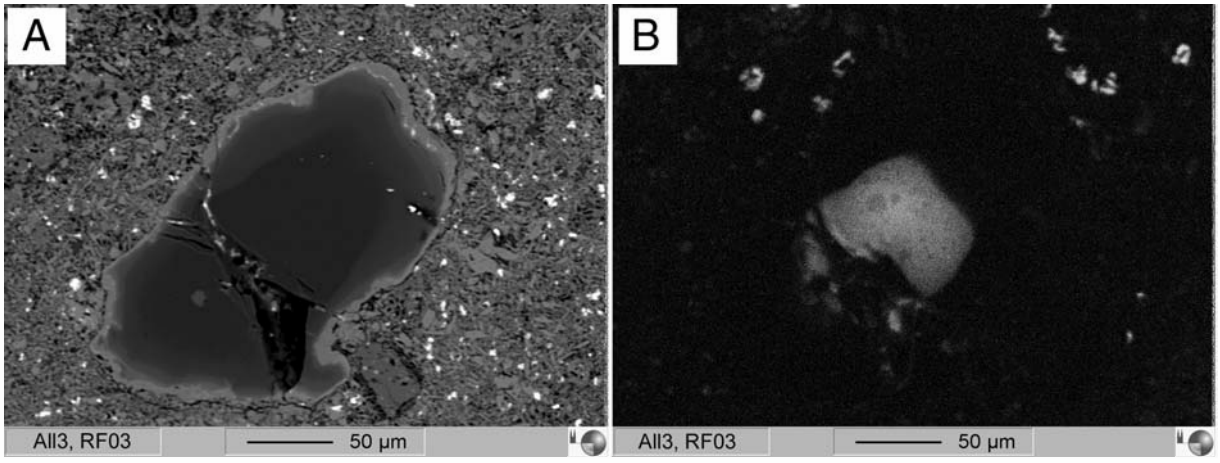


Fig. 1. Isolated refractory forsterite grain from Allende (CV3): a) BSE image showing the dark, FeO poor core and the gray, more ferrous rim; b) CL image of the forsterite grain with the luminescent core.

contained ~19–22 wt% CaO (see discussion in Weinbruch et al. [2000]). Since the cores of RF always show the highest CaO concentrations, we suggest that the initial composition of the parent melt must have been in this range.

Bulk chemical compositions of chondrules were determined by Rubin and Wasson (1987) and Gooding et al. (1983). The highest concentrations of CaO in a chondrule from Allende were reported by Rubin and Wasson (1987) with 10 wt% and by Palme (1990, neutron activation data, personal communication) with 14 wt% CaO. The average CaO content of Allende chondrules is as low as 2.7 wt% (Rubin and Wasson 1987) and 3.8 wt% (Palme 1990, personal communication) and, hence, is not compatible with high CaO contents in RF. To explain this discrepancy, McSween (1977) suggested that the high concentrations of CaO in RF are the result of disequilibrium partitioning of Ca due to the rapid cooling of the chondrule host melt. Chondrules have rapidly cooled from near liquidus temperatures at rates between 10 and 1000°C/hr (Lofgren 1996; see also Hewins 1997; Conolly et al. 1998). Kennedy et al. (1993) demonstrated that rapid cooling, accompanied by rapid growth of olivine, shift partition coefficients toward higher values. Therefore, possibly, the high CaO contents in refractory forsterites are the result of rapid cooling, and experimentally determined equilibrium Ca olivine/melt partition coefficients are not applicable.

## Aim of This Study

We have conducted dynamic crystallization experiments in CMAS and CMAS-Ti systems to test the hypothesis that rapid cooling of a chondrule melt with ~5 to 10 wt% CaO can produce forsterites with 0.6–0.8 wt% CaO. The results of our experiments will be discussed with respect to the formation of refractory forsterites by crystallization from melts.

Preliminary results of this work were presented in Pack et al. (2002a) and Pack and Palme (2002c).

## Olivine/Melt Partitioning

The equilibrium partitioning of Ca between olivine and silicate melts of various compositions was systematically studied by Libourel (1999). He concluded from a large set of experiments, as well as from the study of natural samples, that the Ca partitioning is independent of temperature and oxygen fugacity at a range of 1050 to 1530°C. Libourel (1999) concluded that olivine/melt partition coefficients of Ca in CMAS and CMAS-Ti systems solely depend on the CaO content of the melt. The relation between the CaO content of the melt and the CaO content of the coexisting forsterite is expressed by the empirical relation:

$$CaO_{fo} = 0.087 \times (\exp[0.106 \times CaO_{melt}] - 1)$$

Hence, for CMAS and CMAS-Ti systems, the CaO contents of forsteritic olivines are excellent tracers for the CaO contents of the parental melts. In dynamic crystallization experiments, Kennedy et al. (1993) report $D_{Ca}^{ol/melt}$ values between 0.022 and 0.033 without a pronounced dependence on the cooling rate (0–2191°C/hr, <5 wt% bulk CaO).

Equilibrium partitioning of Al between olivine and silicate melts was studied by Colson et al. (1988), Beattie (1994), and Agee and Walker (1990). Colson et al. (1988) report $D_{Al}^{ol/melt}$ between 0.0029 and 0.0092 (1180–1420°C) and Beattie (1994) reports values between 0.010–0.022 (1190–1495°C). Agee and Walker (1990) report decreasing Al in forsterites with decreasing temperature. This limits the applicability of the Al contents of olivine as a tracer for the Al contents of the parental melts, unless the exact crystallization temperature is known. Kennedy et al. (1993) determined $D_{Al}^{ol/melt}$ values between 0.0042 and 0.011 in experiments with cooling rates between 0 and 2191°C/hr. No systematic dependence of the Al partitioning from the cooling rate is reported by these authors (see Table 5 in Kennedy et al. [1993]).

Dynamic crystallization experiments are used to quantify kinetic effects of element partitioning. For a detailed discussion of kinetic effects on trace element partitioning between melts and crystals, the reader is referred to Brice (1969). Generally, $D_i^{X\text{-tal/melt}}$ will increase with an increasing cooling rate if $D_i^{X\text{-tal/melt}} < 1$ and if the diffusion of (i) in the melt is slow compared to the crystallization speed. Kennedy et al. (1993) showed that the partitioning coefficients of elements like Sr, Ba, and light rare earth elements systematically increase with increasing cooling rates.

## EXPERIMENTAL SETUP

### Dynamic Crystallization Experiments

Eight starting mixtures with CaO contents between 4 and 25 wt% and $Al_2O_3$ contents between 5 and 22 wt% were prepared from analytical grade oxides and carbonates (Table 1). The compositions of the starting mixtures was chosen in such a way that forsterite is the first phase to crystallize.

Mix-01 is the only sample that contains, in addition to CMAS-(Ti), small amounts of FeO, $Cr_2O_3$, and MnO. All other starting mixtures (Mix-03, Mix-04, and Mix-A–Mix-D) are free of Fe, Mn, and Cr considering the low (<1 wt%) concentrations of FeO, MnO, and $Cr_2O_3$ present in meteoritic RFs.

The starting materials were homogenized by fusion in Pt crucibles at 1550°C for 30 min after thoroughly grinding the mixtures for 30 min in an agate mortar. The resulting melts were quenched in air and the glass was re-ground to powder. Splinters of the glass were hand picked and embedded into Epoxy-resin and analyzed by EPMA (see data in Table 1). Only sample Mix-A was not completely molten due to its high liquidus temperature. Therefore, the composition of this mixture was determined from a fused bead by X-ray fluorescence.

The sample powders were pressed to 4 mm (≈2 mm thick) pellets at a load of ≈800 kg in a piston cylinder apparatus. The pellets were stable and the addition of binder was not necessary. The pellets were wound in Pt-loops and placed in a vertical furnace. The temperature in the furnace was determined using a type-B thermocouple, which was calibrated against the melting temperature of Au. The uncertainty of the temperature measurement is estimated to be ±2°C.

An Eurotherm® regulator was used to produce linear temperature ramps between 1.5 and 1000°C/hr. To avoid damage of the heating elements of the furnace, cooling rates were limited to 1000°C/hr. All mixtures were cooled down from ≈1530°C and were quenched in air at a temperature of ≈1050°C.

### Petrography and Electron Microprobe Analyses

For petrographic and mineral chemical analyses, polished sections were prepared from the run products. A JEOL 8900RL electron microprobe was used for back scattered electron (BSE) and cathodoluminescence (CL) imaging, for element distribution mapping (EDM), and for chemical phase analyses. A set of natural and synthetic standards was used for calibration of the wavelength disperse spectrometers. Samples were analyzed at an accelerating potential of 20 kV and a primary beam current of 20 nA.

To test the quality of the EPMA calibration for the low concentrations of CaO and $Al_2O_3$ in the forsterites, several reference samples with known Ca and Al contents were analyzed. Samples SC-1, Mo-22, KH-1, DW/K1, DW/C1, and DW/D1 are mantle peridotities containing olivine, clinopyroxene, orthopyroxene, and spinel.

The CaO data of olivines from various peridotites, SC-1 (0.0767 wt% CaO, SIMS), Mo-22 (0.0836 wt% CaO, SIMS), and KH-1 (0.0889 wt% CaO, EPMA), were taken from Köhler and Brey (1990). The SIMS and the EPMA intensities were calibrated with isotope dilution analyses (IDA). In addition, minerals from peridotite samples DW/K1, DW/C1, and DW/D1 from the Dreiser Weiher (Eifel) were taken as references. These samples had been analyzed previously by Witt-Eickschen (2002, personal communication) by laser ablation ICP-MS. Olivine from sample DW/C1 contains 0.093 wt% CaO, and orthopyroxene from the same rock contains 1.122 wt% CaO. The results are displayed in Fig. 2.

Apparently, no correction of the measured concentrations of CaO had to be applied within a concentration range

Table 1. Chemical compositions of the starting mixtures. The composition was determined by EPMA on quenched samples. Only the composition of Mix-A was determined by XRF.

| Sample | Mix-01 | Mix-03 | Mix-04 | Mix-A | Mix-B | Mix-C | Mix-D | Mix-E |
|---|---|---|---|---|---|---|---|---|
| $SiO_2$ | 46.50 | 47.19 | 45.1 | 48.80 | 52.76 | 48.12 | 46.59 | 42.05 |
| $TiO_2$ | 0.03 | – | – | 2.04 | 2.03 | 2.08 | 1.89 | 2.04 |
| $Al_2O_3$ | 24.74 | 18.62 | 14.3 | 4.99 | 9.55 | 15.10 | 22.03 | 10.33 |
| $Cr_2O_3$ | 0.15 | – | – | – | – | – | – | – |
| FeO | 0.44 | – | – | – | – | – | – | – |
| MnO | 0.16 | – | – | – | – | – | – | – |
| MgO | 21.32 | 16.31 | 18.6 | 39.03 | 26.34 | 22.04 | 13.31 | 19.62 |
| CaO | 7.34 | 17.76 | 22.3 | 4.36 | 8.21 | 12.69 | 15.15 | 25.19 |
| Total | 100.68 | 99.88 | 100.30 | 99.22 | 98.89 | 100.03 | 98.97 | 99.23 |

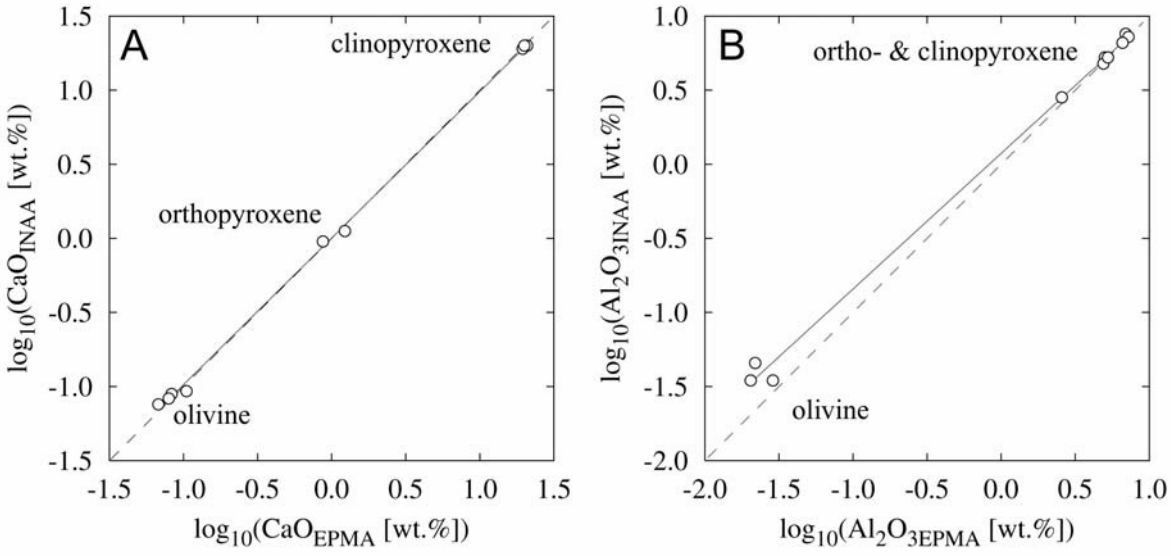


Fig. 2. Plot of "true" versus measured CaO (a) and $Al_2O_3$ (b) concentrations of reference samples. The dashed line displays the 1:1 ratio. The solid lines are best fit regression lines.

between 0.08 and 20 wt% CaO (Fig. 2). The standard deviation of a single CaO analysis in olivine is in the range of ±100 ppm (1σ, sample KH-1, N = 38, 4 different days).

A similar cross check was conducted to test the quality of the Al calibration (neutron activation analyses data from Blum [1982]). In contrast to Ca, a slight deviation from the 1:1 line is observed toward the very low $Al_2O_3$ concentrations in peridotitic olivine (Fig. 2). The best fit line through the data is:

$$\log(Al_2O_{3INAA}[wt\%]) = 0.915 \pm 0.018 \times \log(Al_2O_{3EPMA}[wt\%]) + 0.07 \pm 0.02$$

The measured $Al_2O_3$ data were, therefore, corrected by the relation:

$$Al_2O_{3true}[wt\%] = 10^{0.915 \times \log(Al_2O_{3EPMA}[wt\%])} \times 1.17$$

The standard deviation of a single $Al_2O_3$ analysis is in the range of ±70 ppm (1σ, sample KH-1, N = 38, 4 different days).

The modal compositions given for some of the run products were determined by image analysis on BSE or CL images using the Adobe Photoshop® histogram function (see Fig. 4).

## RESULTS

### Petrography

Donaldson (1976) investigated the morphology of olivine grown in rapidly cooled melts. The terminology for the various olivine morphologies was adopted from this study.

With the exception of sample Mix-A, all samples were heated to super liquidus temperatures so that the concentrations of crystallization seeds was very low or zero. The texture of the experiments with Mix-A is characterized by numerous euhedral and largely isometric forsterite grains (Fig. 4), resembling the texture of porphyritic olivine chondrules. The presence of nucleation sites allows abundant crystals to grow close to equilibrium without extensive undercooling, which is necessary to form stable seeds in a melt devoid of nucleation sites (see Cohen et al. 2000).

Samples that were pre-heated to super-liquidus temperatures show a systematic change in olivine morphology. At low cooling rates, a few large hopper forsterite grains crystallized from the melt (Fig. 3a). With increasing cooling rate, grain sizes and habits of the forsterites change gradually from smaller hopper crystals toward chain olivines (Figs. 3b–3d). The thickness of the chain olivines decreases with increasing cooling rate. The absence of barred olivine textures that are present in many chondrules is notable. This may be the result of the comparatively high Ca and Al contents of our samples.

In most experiments, forsterite is the only crystalline phase. In 4 experimental run products, however, apart from forsterite, also anorthite, pyroxene, and pyroxenoid are observed (Figs. 5a–5d).

In experiment Mix-04 (7.5°C/hr), crystallization of coarse hopper forsterites (25 vol%) was followed by crystallization of coarse aluminous fassaite ($Ca_{0.96}Mg_{0.60}Al_{0.80}Si_{1.62}O_6$, 64 vol%) and bustamite ($Ca_{0.79}Mg_{0.20}Al_{0.38}Si_{0.75}O_3$, ≈7.5 vol%; Fig. 5a). Bustamite crystallized from the residual interstitial melt (≈7.5 vol%). The composition of the melt before crystallization of fassaite and bustamite was recalculated using the modal composition of the run products and the chemical composition of the individual phases.

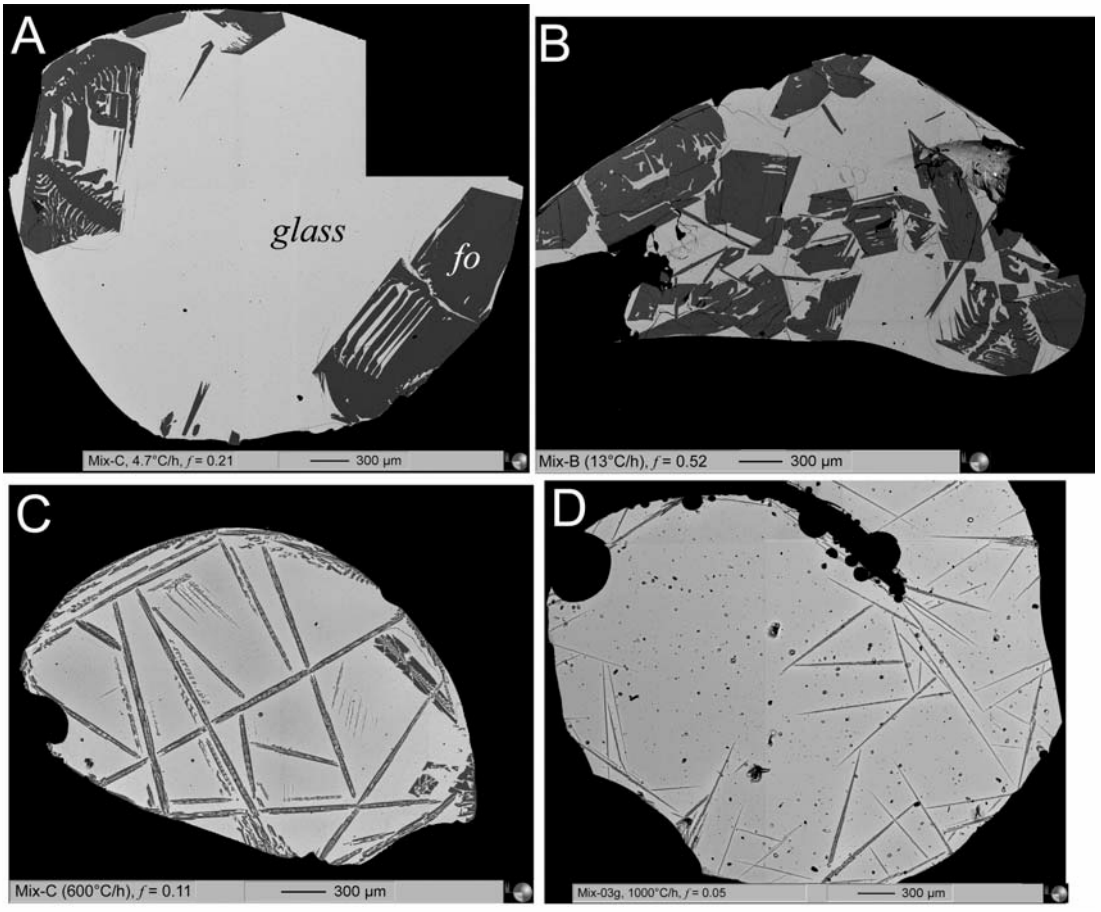


Fig. 3. BSE images of experimental run products that were cooled down at different rates: a) experiment Mix-C (4.7°C/hr) with a few large hopper crystals; b) Mix-B cooled down at 13°C/hr with partly euhedral, partly hopper forsterite crystals; c) experiment Mix-C (600°C/hr) with chain olivines; d) experiment Mix-03 (1000°C/hr) with very thin chain forsterites.

At the liquidus of Mix-D, anorthite, instead of forsterite, is the first phase to crystallize. In the "20% $Al_2O_3$" section of the quaternary CMAS phase diagram, composition Mix-D plots in the forsterite stability field close to the fo-an cotectic line (Fig. 6). The increase in $Al_2O_3$ to 22 wt% (Table 1) leads to a shift of the fo-an cotectic line so that anorthite is the first phase to crystallize. In experiment Mix-D (4.7°C/hr), ophitic anorthite (66 vol%) crystallized before forsterite (15 vol%, Fig. 5b). Since crystallization of forsterite post dates crystallization of anorthite, no correction of the melt composition was applied. In experiment Mix-D (13°C/hr), again, ophitic anorthite (23.5 vol%) crystallized before forsterite. Crystallization of ophitic anorthite was followed by cotectic crystallization of olivine intergrown with anorthite (Fig. 5c).

The melt composition from which forsterite (11 vol%) and anorthite (38.5 vol%) cotectically crystallized was recalculated by subtracting the amount of ophitic forsterite (23.5 vol%) from the bulk composition using image analysis. The change in CaO content, however, is only minor (+1.6 wt%) and, therefore, is not outlined in Fig. 13. Experiment Mix-D (600°C/hr) is entirely glassy without any crystalline phase, and Mix-D (1000°C/hr) contains only very small anorthite crystals but no forsterite.

In Mix-E (13°C/hr), coarse grained fassaite ($Ca_{1.01}Mg_{0.69}Al_{0.62}Si_{1.59}O_6$, 40 vol%) crystallized after forsterite (47 vol%) from the residual melt (13 vol%; Fig. 5d). The difference between measured (light gray) and recalculated melt compositions are outlined in Fig. 13 by horizontal arrows.

## Cathodoluminescence

In all the experiments, forsterite exhibits blue CL, as identified by using the color video camera attached to the JEOL probe. With respect to the CL, the experimentally grown forsterites resemble the luminescent meteoritic RF grains. The overall CL intensity increases with the increasing Ca, Al, and Ti contents of the forsterites. The highest CL intensity (close to being off the scale of the CL detection unit) was observed in the CMAS-Ti experiments, indicating that Ti is a very strong CL activator.

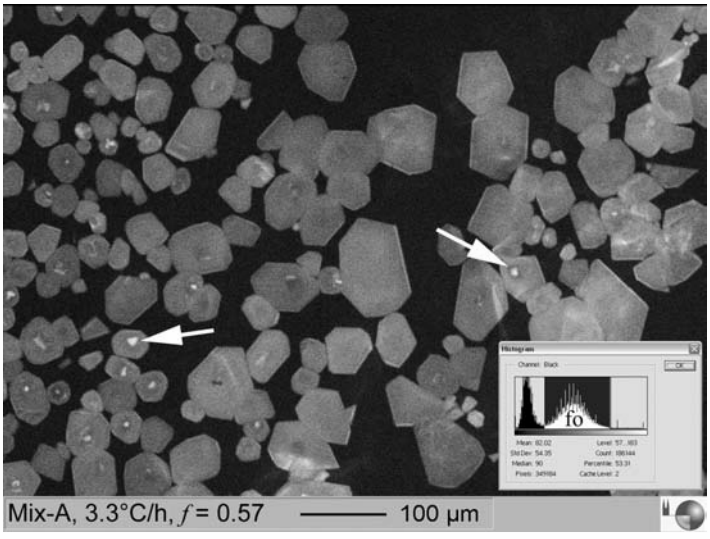


Fig. 4. CL image showing experiment Mix-04 cooled down at 3.3°C/hr. The forsterites show a weak overall CL intensity but are well-visible within the nonluminous glass matrix. Due to the presence of abundant crystallization seeds (arrows), a porphyritic texture has developed. The fraction of forsterite was determined by image analyses using the Adobe Photoshop® histogram function (see detail).

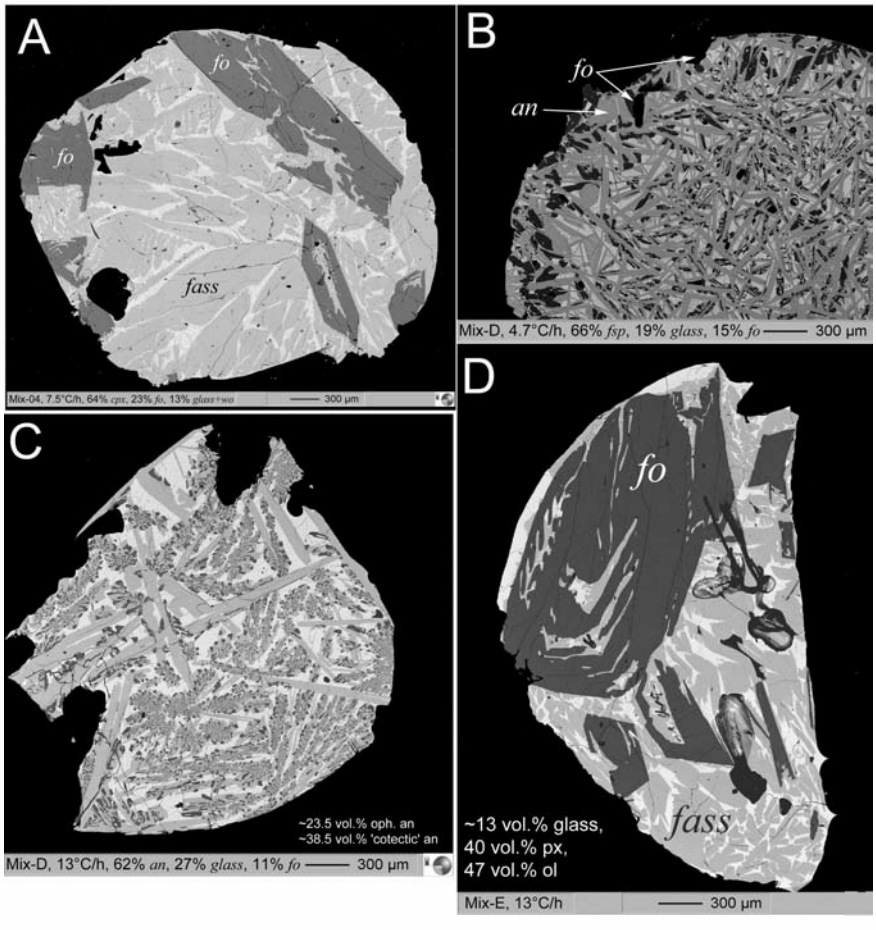


Fig. 5. BSE images of run products with other crystalline phases besides forsterite: a) experiment Mix-04 (7.5°C) with hopper forsterites, fassaite, and interstitially intergrown bustamite and melt; b) in experiment Mix-D (4.7°C) ophitic anorthite crystallized before forsterite; c) Mix-D cooled at 13°C/hr with ophitic anorthite and eutectically intergrown anorthite and forsterite and interstitial melt; d) Mix-E (13°C/hr) with large hopper forsterites, fassaite, and glassy mesostasis.

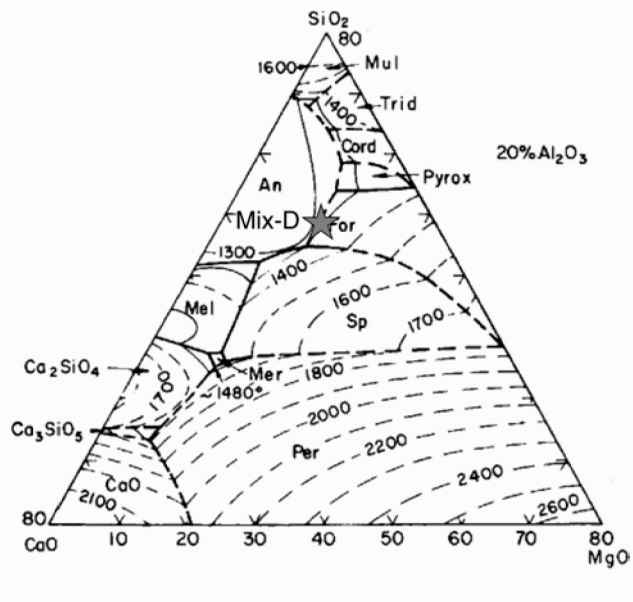


Fig. 6. Quaternary phase diagram $SiO_2$, CaO, MgO + 20% $Al_2O_3$. The composition of Mix-D plots close to the fo-an cotectic line. At 22 wt% $Al_2O_3$ (see Table 1), Mix-D plots to the "left" of the cotectic line within the stability field of anorthite (after Osborn et al. [1954]).

The majority of the forsterite grains exhibit heterogeneous CL distribution. Fig. 8 shows a CL image of a forsterite (Mix-03) grown at a cooling rate of 1.5°C/hr. The core of the grain shows the brightest CL-emission, while the discontinuous rims is significantly less luminescent.

CL reveals different zones, which are separated from each other by sharp but curved contacts (Figs. 7a and 7b). This suggests that the olivine grains do not continuously crystallize but grow in discrete "steps" at different temperatures. The outermost zone ("3" and "B" in Fig. 7a; "2" in Fig. 7b) with the lowest CL intensity may have crystallized during quenching. The "tail" at the edge of the olivine grain (arrows Fig. 7a), however, probably did form during the crystallization of zone "3" and is, thus, not a product of quenching. The glass devitrified during quenching in air.

Chemical profiles reveal Al to be the predominant CL activating element in the $TiO_2$-free sample Mix-03 (1.5°C/hr). A similar relation between CL intensity and Al content was reported by Pack et al. (Forthcoming) for a refractory forsterite grain from R chondrite Dar al Gani 013. The concentration of Al decreases at the contact between the zone with bright CL and the almost non-luminous rims (Figs. 7a–7d). In contrast to Al, discontinuous changes of the CaO contents at the boundaries defined by CL are not observed.

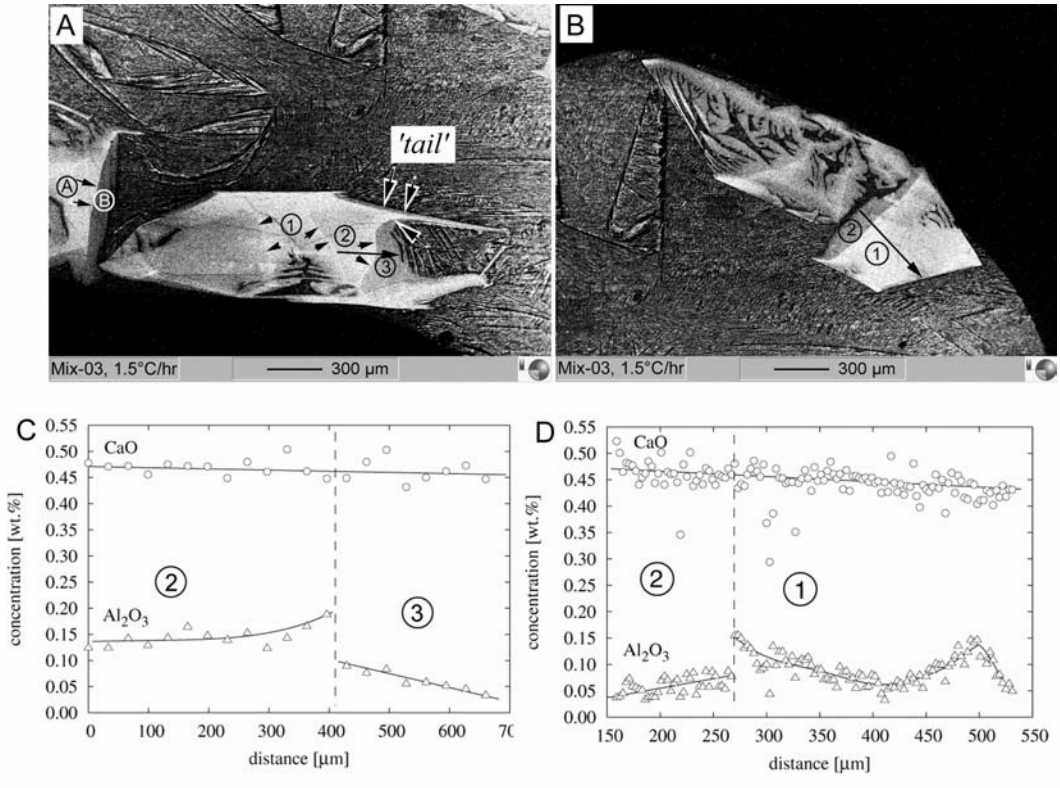


Fig. 7. a) and b) CL images showing irregularly shaped hopper forsterites with heterogeneous CL distribution (Mix-03, 1.5°C/hr). The glass is devitrified. Note the sharp, curved contact between the different CL zones within the forsterite grains (arrows); c) and d) chemical profiles were measured across the boundary between the zones with different CL intensities.

High concentrations of CaO in forsterite do not lead to intense luminescence. The continuous decrease in Al toward the outermost rim may be related to the decreasing crystallization temperature. Agee and Walker (1990) have demonstrated that the Al partition coefficient decreases with decreasing temperature.

**Element Distribution Maps**

Element distribution maps (EDMs) are valuable tools to quantify the homogeneity of the experimental run products. The intensities of the X-ray lines are assumed to be proportional to the concentrations of the individual element within an individual phase (glass, forsterite).

Fig. 8 shows a small euhedral forsterite from experiment Mix-04 (4.7°C/hr) with well-developed "sand clock"-like sector zoning in CL (see Fig. 8d). The enhanced luminescence along the {010} prism faces is related to preferable incorporation of Ti and Al relative to the {021} faces (arrows, Figs. 8a and 8b). Ca, apparently, does not show any preferable incorporation along the prism faces and is largely homogenously distributed throughout the grain, although the intensity of the Ca-Kα line is about a factor of 2 higher than the Al- and Ti-Kα lines. This type of sector zoning is related to the {hkl} dependence of the interface partitioning coefficient and not to "kinetic effects." The different crystal faces ({010} and {021}) apparently crystallized equally fast, as is indicated by the similar sizes of the crystal faces. Therefore, the built up

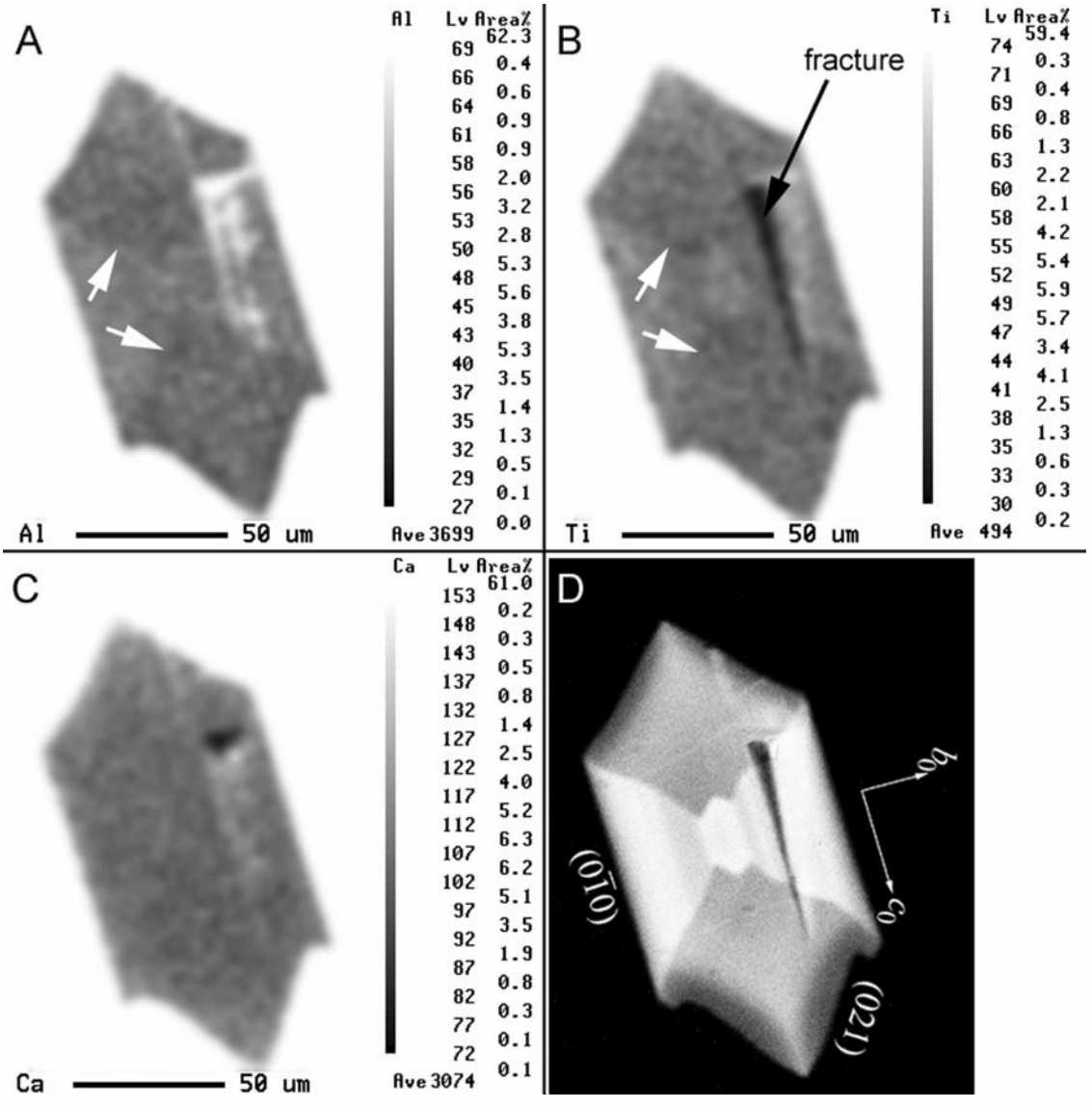


Fig. 8. Al, Ti, and Ca element distribution maps (a–c) and CL image (d) of a zoned forsterite grain from experiment Mix-04 (4.7°C/hr). For noise reduction, the EDMs were Gaussian blurred. Note the sector zoning in Al and Ti (arrows in [a] and [b]), which corresponds to the CL zoning (EDM settings: Kα-lines, 20 kV, 175 nA, 300 ms/pixel, 120 × 180 pixel).

of a moving diffusion boundary is not regarded to be responsible for the sector zoning. The sharp contact between the high-CL and low-CL zones, furthermore, indicates that the annealing time was not sufficiently long to redistribute Al and Ti throughout the grain.

The deviation of the trace element partitioning from equilibrium in dynamic systems can also be related to the build up of moving diffusion layers in front of moving crystal to melt interfaces. If equilibration through diffusion and convection in the melt is an effective process, melts will be homogenous in composition even very close to the crystals. If the growth rate of the crystals exceed the efficiency of the melt to homogenize, trace element contents will increase at the crystal to melt interface, i.e., a diffusion layer will form. The degree of concentration increase toward the crystal to melt interface depends on the diffusivity of the individual element within the melt and the difference in concentration between crystal and melt. The less effective the homogenization process is, the more heterogeneous the melt will be.

The "degree of heterogeneity" ($h_i$) of element (i) in the melt was calculated from the element distribution maps. $h_i$ within an area section is defined as:

$$h_i = 100 \times \left( \frac{I_i^{max} - I_i^{min}}{I_i^{*}} \right)$$

The intensities $I_i^{min}$ and $I_i^{max}$ are the minimum and the maximum intensities of element (i) in counts per pixel. $I_i^{*}$ is the intensity at the maximum of the intensity distribution histogram of component (i) in the recorded area.

The element distribution maps clearly illustrate that the distribution of Ca within the melt is very homogenous as compared to Al (Fig. 9; Fig. 10). Al significantly increases toward the forsterite to melt contact (Fig. 9; Fig. 10). The increase in Al is related to the build up of a moving diffusion boundary during growth of the forsterites. In the case of Ca, no such diffusion boundary is observed. This indicates that transport of Ca away from the crystal to melt interface is much more effective than that of Al.

Using image analysis, the heterogeneity of the melt in the recorded area sections was quantified. The values for $h_{Ca}$ vary between 5 and 10% for the melt in the areas displayed in Figs. 9 and 10. In the same area sections, Al is much more heterogeneous with $h_{Al}$ varying between 11 and 30% (Fig. 11).

The heterogeneity of Ca and Al within a single forsterite was determined using the EDMs displayed in Figs. 10a and 10e and Figs. 10c and 10g, respectively. Ca appears homogeneously distributed throughout the forsterite grains, while Al shows systematic zoning ($h_{Al}$ = 58%; Fig. 10c). The decrease in Al toward the outer rim is probably related to different growth temperatures (see also Fig. 7).

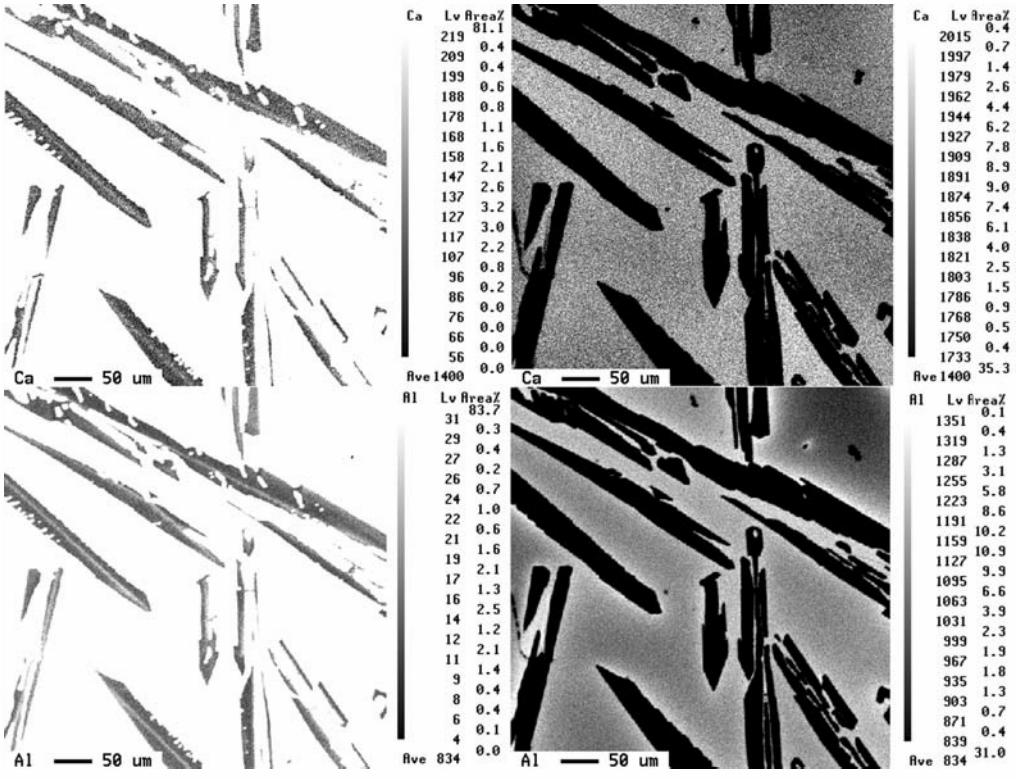


Fig. 9. Ca-Kα (left) and Al-Kα (right) element distribution maps. The intensities of the images were chosen in such a way that maximum grayscale contrast is obtained in the glass: a) and b) Mix-04 (1000°C/hr, EDM settings: 20 kV, 20 nA, 1000 ms/pixel, 150 ×1 50 pixel); c) and d) Mix-E (600°C/hr, EDM settings: 15 kV, 100 nA, 100 ms/pixel, 500 × 500 pixel).

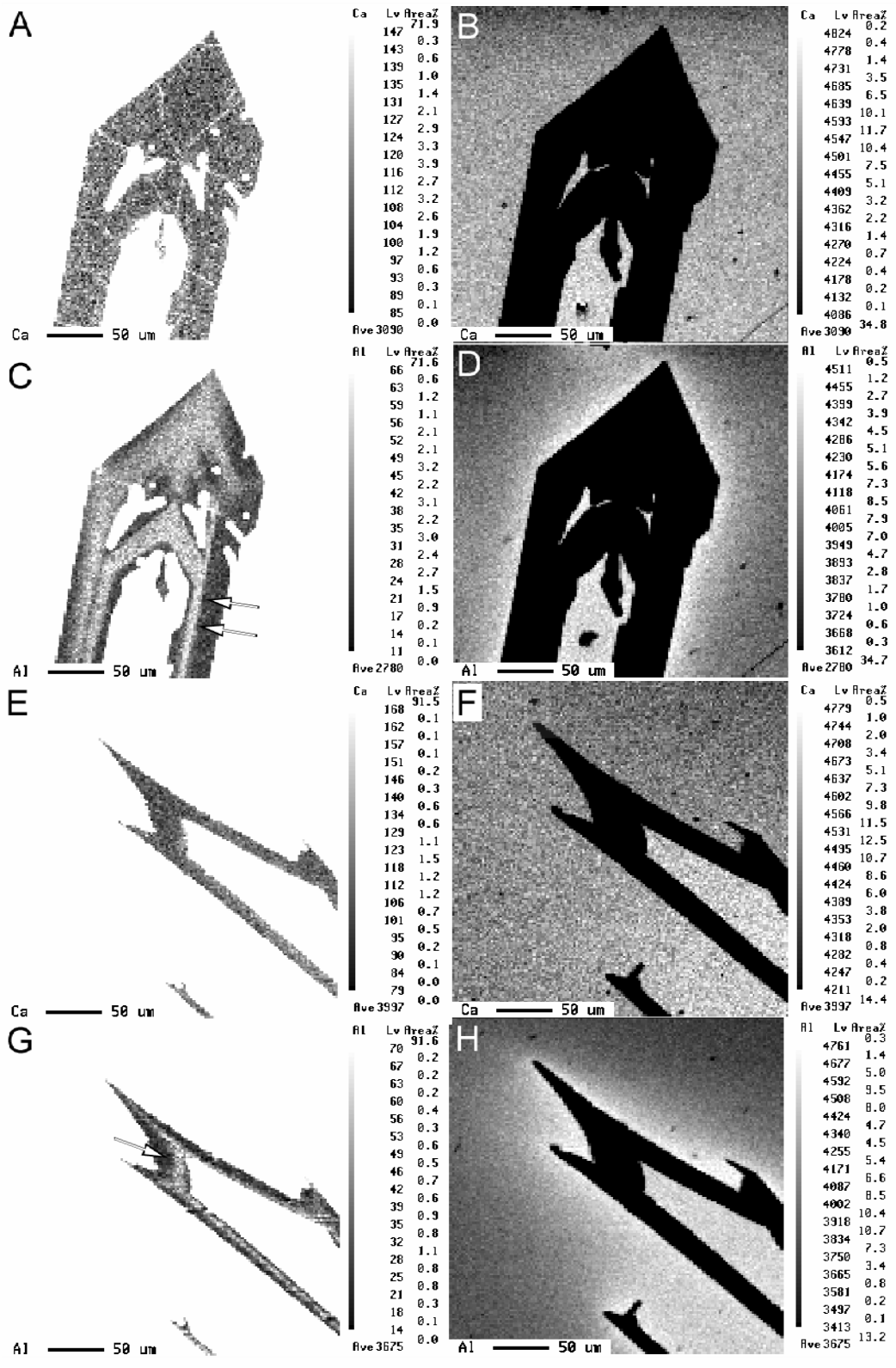


Fig. 10. Element distribution maps (Ca-Kα, Al-Kα) in the melt (b, d, f, h) and in forsterite (a, c, e, g) in experiment Mix-01 (200°C/hr). The gray scale levels were optimized for forsterite (left) and melt (right) using the JEOL image evaluation software (EDM settings: 20 kV, 20 nA, 1000 ms/pixel, 150 × 150 pixel). Note the heterogeneity of Al in the forsterite crystals (arrows in [c] and [g]).

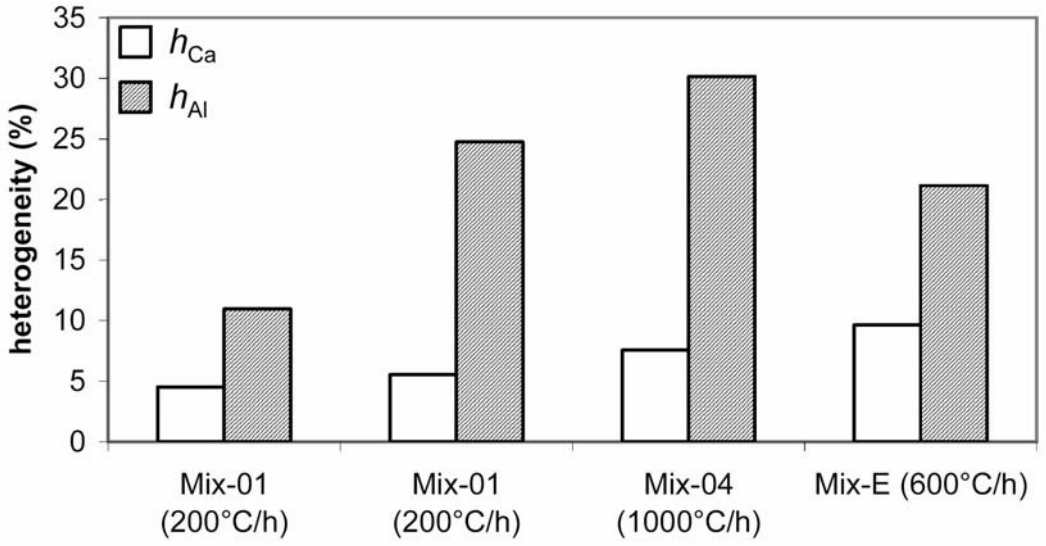


Fig. 11. Plot of the heterogeneity index ($h_i$) in percent of Ca and Al from the same areas. The heterogeneity of Al is in all samples considerably higher than the heterogeneity of Ca (Mix-01, 200°C/hr from Fig. 10; Mix-04, 1000°C/hr and Mix-E, 600°C/hr from Fig. 9).

To resolve the effect of crystallographic orientation (different growth rates) on the partitioning of Ca and Al, 2 chemical profiles were measured across different phase boundaries in the run product from a single experiment (Mix-01, 200°C/hr). One profile was measured perpendicular to a well-developed forsterite crystal face, i.e., a slowly moving phase boundary (Figs. 12a and 12c). A second profile was measured across a small crystal face that is regarded to have moved rapidly (Figs. 12b and 12d).

No diffusion boundaries in Si, Al, Mg, and Ca are observed in the melt adjacent to the well-developed crystal faces and, hence, adjacent to the slowly moving phase boundary (Fig. 12c). The phase boundary is apparently equilibrated and no deviation from equilibrium partitioning is expected, although the sample was cooled at a rate of 200°C/hr. In the case of the fast growing face (Figs. 12b and 12d), a slight increase in CaO in the melt from 9 wt% to 10 wt% toward the phase boundary is observed. The concentration of $Al_2O_3$ increases considerably from 18 to 25 wt% toward the phase boundary. Apparently, diffusive and/or convective transport of Al is slower than the growth rate of the specific crystal face. The thickness ($\delta$) of the moving boundary is approximately 20 µm. The same is true for Mg, which decreases towards the melt contact because $D_{Mg}^{ol/melt} > 1$. The concentration of $SiO_2$ increases slightly toward the phase boundary.

Above, we showed that differences in the interface partitioning coefficient can result in sector zoning (see Fig. 8). Differences in the growth rate of individual crystal faces can also produce sector zoning. Fig. 12 is an example for potential sector zoning due to differences in the growth rates of various crystal faces. In front of fast moving faces, diffusion boundaries will build up, while slowly moving crystal faces will be in equilibrium with the melt. Fig. 12 also demonstrates that the diffusion of Al within the silicate melt is less effective compared to Ca, confirming the observations made in EDMs.

## Olivine/Melt Partition Coefficients (Al, Ca)

The partitioning coefficients were determined by measuring a number of randomly selected EPMA spots on forsterite and glass of the experimental run products (Table 2).

To avoid phase boundary fluorescence (PBF) effects, forsterite analyses were done at least ≈20 µm away from the rim. With respect to PBF, determination of the composition of the chain forsterites was problematic. Finding sufficiently wide (≈20–30 µm) undisturbed areas on sections of these forsterites for EPMA and fully avoiding PBF proved to be difficult. Therefore, for experiments with cooling rates ≥600°C/hr, the lowest Ca and Al, instead of the mean concentration analyzed, were assumed to best represent the true composition of the forsterite (see Fig. 13). Those analyses with the lowest concentrations of CaO and $Al_2O_3$ are regarded to be least affected by PBF. Single outliers with extremely low concentrations of CaO and $Al_2O_3$, however, were not considered.

### *Calcium*

Figure 13 is a plot of CaO concentrations in experimentally grown forsterites versus the bulk CaO concentration in the starting mixtures (solid symbols) and the CaO contents of the co-existing melts (open symbols). In some experiments (Mix-E, 13°C/hr; Mix-04, 7.5°C/hr), crystallization of olivine was followed by other phases (anorthite, pyroxene, pyroxenoid). Based on the modal compositions as determined by image analyses, the compositions of the melts were recalculated to obtain the composition of the melt that co-existed with the

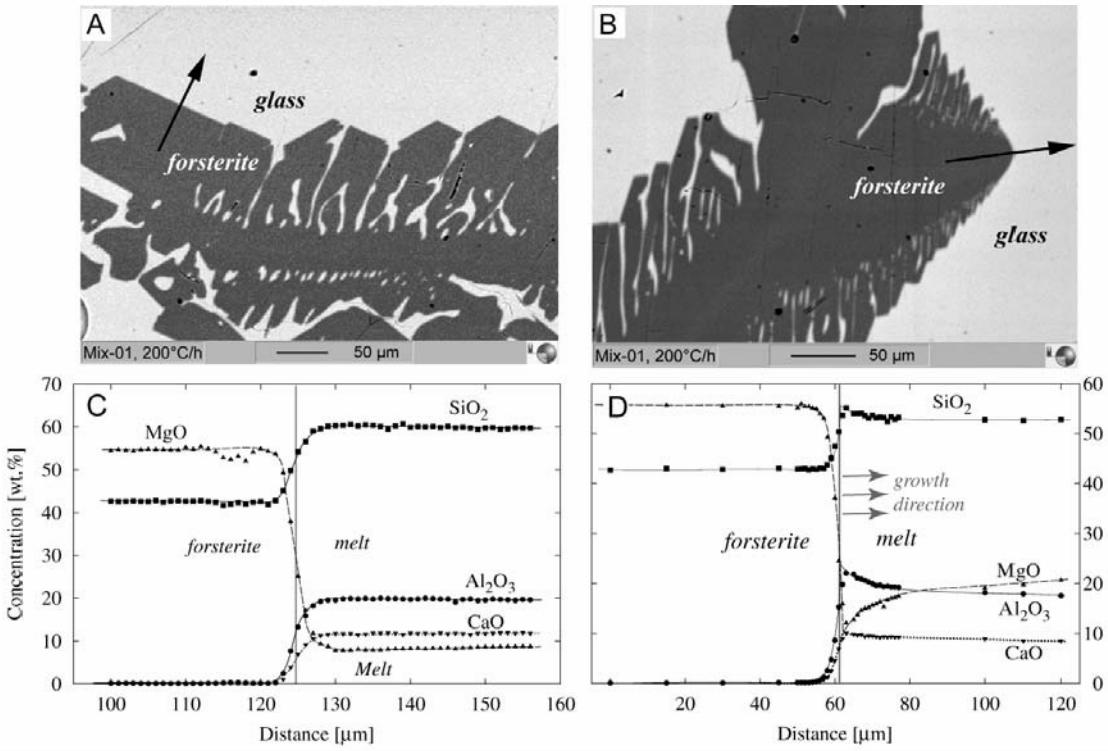


Fig. 12. BSE images and EPMA profiles across an olivine to melt boundary from experiment Mix-01 (200°C/hr): a) skeletal forsterite with the position of the EPMA profile across a large crystal face outlined; b) skeletal forsterite with a profile across a fast moving phase boundary indicated; c) the melt is homogenous adjacent the large, i.e., slowly moving crystal face; d) a moving diffusion layer built up in front of a small, i.e., fast growing crystal face. The thickness of the diffusion layer is $\delta \approx 20$ µm.

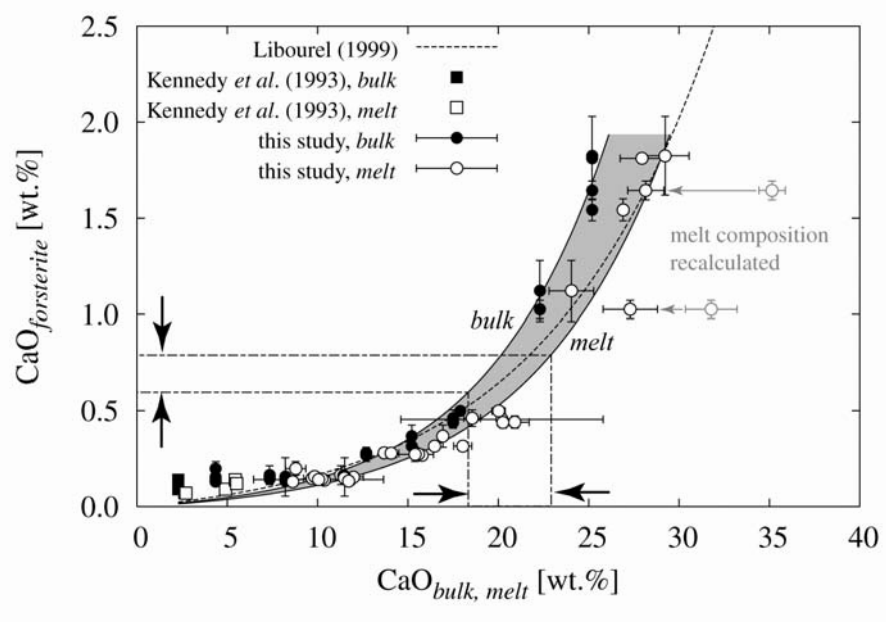


Fig. 13. Plot of CaO in forsterite verus bulk CaO (solid symbols) and CaO in the co-existing melt (open symbols). The squares are data from Kennedy et al. (1993). The dashed curve is from Libourel (1999, equilibrium). The melt compositions of Mix-E (13°C/hr) and Mix-04 (7.5°C/hr) were recalculated based on modal compositions (gray symbols). The gray shaded area marks the borders of the "bulk curve" and the "melt curve," where "bulk" refers to the CaO content of the starting material and "melt" to the CaO content of the melt between the forsterite crystals.

Table 2. EPMA analyses of the run products of dynamic crystallization experiments. The numbers in parentheses are the number of analyses.

| | ΔT/Δt | T-start | CaO (wt%) | | | | | | | | $Al_2O_3$ (wt%) | | | | | | | | |
|---|---|---|---|---|---|---|---|---|---|---|---|---|---|---|---|---|---|---|---|
| Sample | (°C/hr) | (°C) | gl | 1σ | N | ol | 1σ | N | $D^{ol/melt}$ | 1σ | gl | 1σ | N | ol | 1σ | N | $D^{ol/melt}$ | 1σ | Assemblage |
| Mix-A | 0 | 1530 | 8.8 | 0.6 | (6) | 0.20 | 0.04 | (9) | 0.024 | 0.004 | 9.2 | 1.0 | (6) | 0.08 | 0.03 | (9) | 0.009 | 0.003 | gl, fo |
| Mix-A | 3.3 | 1530 | 8.61 | 0.06 | (10) | 0.13 | 0.01 | (6) | 0.016 | 0.001 | 9.81 | 0.06 | (10) | 0.051 | 0.003 | (6) | 0.0052 | 0.0003 | gl, fo |
| Mix-A | 4.7 | 1530 | 11.49 | 0.07 | (13) | 0.15 | 0.01 | (26) | 0.0146 | 0.0008 | 13.94 | 0.08 | (13) | 0.054 | 0.004 | (26) | 0.0039 | 0.0003 | gl, fo |
| Mix-A | 13 | 1530 | 10.4 | 0.1 | (7) | 0.14 | 0.01 | (7) | 0.014 | 0.001 | 11.76 | 0.05 | (7) | 0.047 | 0.004 | (7) | 0.0040 | 0.0004 | gl, fo |
| Mix-01 | 20 | 1530 | 11.3 | 0.2 | (18) | 0.16 | 0.05 | (24) | 0.016 | 0.004 | 24.1 | 0.7 | (18) | 0.26 | 0.09 | (24) | 0.011 | 0.004 | gl, fo |
| Mix-01 | 20 | 1530 | 9.7 | 0.5 | (26) | 0.15 | 0.01 | (13) | 0.014 | 0.001 | 19.4 | 1.5 | (26) | 0.25 | 0.02 | (13) | 0.0127 | 0.0009 | gl, fo |
| Mix-01 | 20 | 1530 | 10.2 | 0.4 | (17) | 0.14 | 0.01 | (14) | 0.015 | 0.001 | 18.1 | 0.6 | (17) | 0.21 | 0.03 | (14) | 0.012 | 0.002 | gl, fo |
| Mix-01 | 200 | 1530 | 12.0 | 0.5 | (27) | 0.15 | 0.02 | (23) | 0.016 | 0.002 | 19.7 | 1.0 | (27) | 0.10 | 0.08 | (23) | 0.005 | 0.004 | gl, fo |
| Mix-01 | 200 | 1530 | 11.4 | 0.4 | (14) | 0.16 | 0.01 | (25) | 0.015 | 0.001 | 21.5 | 1.0 | (14) | 0.11 | 0.06 | (25) | 0.005 | 0.003 | gl, fo |
| Mix-B | 3.3 | 1530 | 9.83 | 0.06 | (7) | 0.156 | 0.005 | (7) | 0.0173 | 0.0005 | 11.48 | 0.04 | (7) | 0.054 | 0.004 | (7) | 0.0047 | 0.0003 | gl, fo |
| Mix-B | 4.7 | 1530 | 11.49 | 0.07 | (10) | 0.2 | 0.1 | (31) | 0.015 | 0.009 | 13.8 | 0.6 | (10) | 0.054 | 0.004 | (31) | 0.0039 | 0.0004 | gl, fo |
| Mix-B | 13 | 1530 | 11.47 | 0.06 | (7) | 0.149 | 0.006 | (9) | 0.0141 | 0.0005 | 13.5 | 0.3 | (7) | 0.049 | 0.007 | (9) | 0.0036 | 0.0006 | gl, fo |
| Mix-B[a] | 600 | 1530 | 11.7 | 0.3 | (9) | 0.13 | 0.01 | (7) | 0.012 | 0.001 | 12.8 | 0.7 | (9) | 0.05 | 0.01 | (7) | 0.004 | 0.001 | gl, fo |
| Mix-B[a] | 1000 | 1530 | 10.1 | 3.6 | (15) | 0.14 | 0.01 | (8) | 0.015 | 0.005 | 10.4 | 3.2 | (15) | 0.064 | 0.009 | (8) | 0.006 | 0.002 | gl, fo |
| Mix-C | 3.3 | 1530 | 13.68 | 0.04 | (5) | 0.281 | 0.007 | (7) | 0.0223 | 0.0005 | 16.42 | 0.05 | (5) | 0.14 | 0.02 | (7) | 0.0085 | 0.0009 | gl, fo |
| Mix-C | 4.7 | 1530 | 15.79 | 0.08 | (5) | 0.27 | 0.01 | (14) | 0.0184 | 0.0007 | 18.84 | 0.09 | (5) | 0.11 | 0.02 | (14) | 0.006 | 0.001 | gl, fo |
| Mix-C | 13 | 1530 | 15.59 | 0.06 | (9) | 0.27 | 0.01 | (12) | 0.0190 | 0.0008 | 18.5 | 0.1 | (9) | 0.14 | 0.01 | (12) | 0.0077 | 0.0007 | gl, fo |
| Mix-C[a] | 600 | 1530 | 15.4 | 1.0 | (7) | 0.27 | 0.04 | (17) | 0.019 | 0.003 | 17.6 | 1.0 | (7) | 0.19 | 0.05 | (17) | 0.011 | 0.003 | gl, fo |
| Mix-C[a] | 1000 | 1530 | 14.1 | 0.4 | (6) | 0.28 | 0.02 | (8) | 0.021 | 0.002 | 15.9 | 0.3 | (6) | 0.30 | 0.04 | (8) | 0.019 | 0.003 | gl, fo |
| Mix-D | 4.7 | 1530 | 16.9 | 0.1 | (5) | 0.37 | 0.06 | (9) | 0.024 | 0.003 | 10.74 | 0.08 | (5) | 0.11 | 0.04 | (9) | 0.011 | 0.004 | gl, fo, an |
| Mix-D[b] | 13 | 1530 | 18.0 | 0.5 | (7) | 0.32 | 0.02 | (8) | 0.019 | 0.001 | 22.7 | 0.5 | (7) | 0.07 | 0.01 | (8) | 0.0030 | 0.0005 | gl, fo, an |
| Mix-03 | 1.5 | 1530 | 20.9 | 0.8 | (17) | 0.44 | 0.03 | (25) | 0.023 | 0.002 | 21 | 3 | (17) | 0.15 | 0.04 | (25) | 0.007 | 0.002 | gl, fo |
| Mix-03 | 1.5 | 1530 | 20.2 | 5.6 | (49) | 0.45 | 0.03 | (35) | 0.024 | 0.006 | 22 | 9 | (49) | 0.11 | 0.03 | (35) | 0.005 | 0.002 | gl, fo |
| Mix-03 | 14.6 | 1530 | 20.3 | 0.3 | (13) | 0.44 | 0.03 | (20) | 0.023 | 0.002 | 20.2 | 0.4 | (13) | 0.30 | 0.03 | (20) | 0.015 | 0.001 | gl, fo |
| Mix-03 | 200 | 1530 | 20.0 | 0.4 | (12) | 0.50 | 0.02 | (10) | 0.027 | 0.001 | 19.2 | 0.9 | (12) | 0.21 | 0.05 | (10) | 0.011 | 0.003 | gl, fo |
| Mix-03 | 300 | 1530 | 18.5 | 0.5 | (12) | 0.46 | 0.04 | (11) | 0.027 | 0.002 | 18.6 | 0.3 | (12) | 0.33 | 0.08 | (11) | 0.017 | 0.004 | gl, fo |
| Mix-04[b] | 7.5 | 1530 | 27.3 | 1.5 | (15) | 1.03 | 0.05 | (109) | 0.038 | 0.003 | 18.5 | 0.8 | (15) | 0.29 | 0.08 | (109) | 0.016 | 0.004 | gl, fo, px, bust |
| Mix-04[a] | 1000 | 1530 | 24.0 | 1.2 | (8) | 1.1 | 0.2 | (9) | 0.047 | 0.007 | 15.7 | 1.0 | (8) | 0.31 | 0.08 | (9) | 0.020 | 0.005 | gl, fo |
| Mix-E | 3.3 | 1530 | 26.90 | 0.09 | (7) | 1.54 | 0.06 | (8) | 0.057 | 0.002 | 11.18 | 0.03 | (7) | 0.16 | 0.03 | (8) | 0.014 | 0.002 | gl, fo |
| Mix-E[b] | 13 | 1530 | 28.2 | 1.0 | (6) | 1.64 | 0.05 | (7) | 0.058 | 0.003 | 14.6 | 0.5 | (6) | 0.13 | 0.03 | (7) | 0.009 | 0.002 | gl, fo, px |
| Mix-E[a] | 600 | 1530 | 29.2 | 1.3 | (6) | 1.8 | 0.2 | (8) | 0.062 | 0.008 | 11.7 | 0.6 | (6) | 0.15 | 0.05 | (8) | 0.013 | 0.005 | gl, fo |
| Mix-E[a] | 1000 | 1530 | 28.0 | 1.2 | (7) | 1.81 | 0.02 | (6) | 0.065 | 0.003 | 11.0 | 0.3 | (7) | 0.167 | 0.006 | (6) | 0.0152 | 0.0007 | gl, fo |

[a]Minimum CaO of forsterite.

[b]Melt composition recalculated.

olivine before crystallization of anorthite, pyroxene, or pyroxenoid. The data with recalculated melt compositions are indicated in Table 2 and Fig. 13.

In dynamic crystallization experiments, equilibrium between forsterite and residual melt may only partly be achieved. Therefore, 2 extreme curves are displayed in Fig. 13. The "bulk curve" is calculated from the CaO contents of the forsterites and the CaO contents of the starting mixtures. The best fit through these data is expressed as:

$$CaO_{forsterite} = 0.041 \times \exp(0.132 \times CaO_{bulk}) - 1$$

The "melt curve" is calculated from the CaO contents of forsterites and the coexisting melts and is expressed as:

$$CaO_{forsterite} = 0.045 \times \exp(0.145 \times CaO_{bulk}) - 1$$

Relative to the equilibrium curve (dashed line), no significant increase in the Ca partitioning coefficient is observed (Fig. 13). No significant increase of $D_{Ca}^{ol/melt}$ with an increasing cooling rate and increasing CaO content of the melt is observed.

### *Aluminum*

No apparent simple relationship exists between the Al partition coefficient and the melt composition. The temperature dependence of the Al-partitioning (Agee and Walker 1990) and the heterogeneity of Al within the forsterites and the melt furthermore complicates the partitioning behavior of Al. Kennedy et al. (1993), in their dynamic crystallization experiments, gave a range between 0.004 and 0.01. In our experiments, the "bulk" and the "melt" Al partition coefficients vary by almost 1 order of magnitude between 0.003 and 0.02 (Fig. 14).

## Summary

Our dynamic crystallization experiments demonstrate that luminescent forsterites can be grown experimentally in CMAS and CMAS-Ti systems. The CL intensity appears to be related to the Al and Ti concentrations in the forsterites. The concentration of Ca in the forsterites has no influence on the CL intensity. The highest CL intensity is observed in Ti-bearing forsterites from experiments in CMAS-Ti systems.

Textures resembling those of porphyritic olivine chondrules were obtained only from experiments with Mix-A. The appearance of porphyritic olivine textures is clearly related to the presence of crystallization nuclei at the beginning of the run. In experiments with high cooling rates, chain forsterites, instead of barred olivines, crystallized. The absence of true barred olivine textures may be related to compositional differences (e.g., FeO content) between barred olivine chondrules from chondrites and our experiments. Forsterites from our experiments resemble luminescent RF from chondritic meteorites.

We demonstrate that Ca partitioning is largely independent of the cooling rate within the range of 1.5 to 1000°C/hr and bulk CaO contents from 5 to 25 wt%. Even at high cooling rates and high bulk CaO, no significant deviation from equilibrium partitioning was found in our experiments. Considering the maximal possible partition coefficient

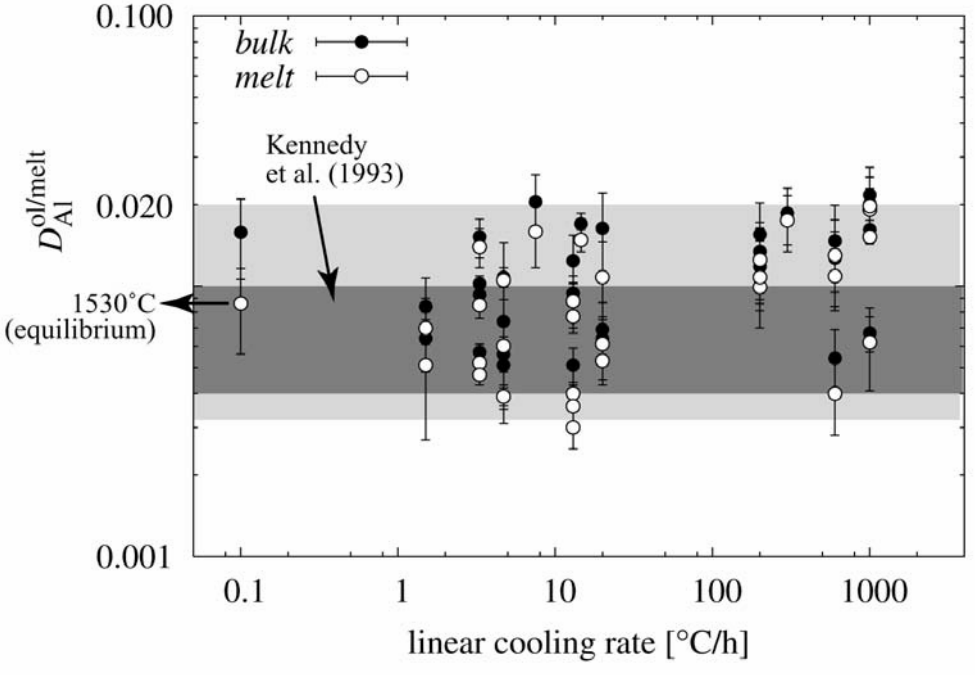


Fig. 14. Plot of $D_{Al}^{ol/melt}$ versus the linear cooling rate. The gray shaded area is within the range of $D_{Al}^{ol/melt}$ from Kennedy et al. (1993).

($D_{Ca}^{ol/melt}$, "bulk curve" in Fig. 13), forsterite with 0.6 to 0.8 wt% CaO can only crystallize from a melt with at least 18.4 to 20.2 wt% CaO, respectively. Our results are in agreement with data from dynamic crystallization experiments done by Kennedy et al. (1993). These authors have conducted experiments in systems with <5 wt% CaO and at cooling rates between 0 and 2193°C/hr. As in our experiments, no systematic changes in the Ca partition coefficient with increasing cooling rate was observed.

We, therefore, suggest that the CaO content of forsteritic olivine is an excellent proxy to trace the CaO content of the parent melt, even in rapidly cooling systems (e.g., chondrules). The validity of our experimental data, however, is restricted to very FeO-poor and alkali-free CMAS and CMAS-Ti melts.

The partitioning behavior of Al is more complex due to: a) the temperature dependence of the partition coefficient; b) the heterogeneity of the melt; and c) the heterogeneity of the forsterite grains (e.g., sector zoning, stepwise growth). Thus, our experiments show that the Al content of forsterite is not a suitable tracer for the composition of the parent melt.

## Application of the Ca-Partition Data to the Problem of RF Formation

The result of this study shows that a magmatic origin of RF with 0.6–0.8 wt% CaO requires a melt with 18–20 wt% CaO. Libourel (1999) has, however, demonstrated that Ca-partitioning into olivine increases in CMAS systems with Na. Thus, the parent liquid of a refractory forsterite could have less than 20 wt% CaO, if the melt from which the forsterite crystallized is Na-rich. Part of our ongoing study is to study the partitioning of Ca and Na between silicate melt (CMAS-Ti) and forsterite. The Na content of RF will then allow us to determine if RF has crystallized in pure CMAS-(Ti) or in alkali-bearing systems. Since RF are, by their very refractory nature, poor in volatile elements, we expect a Na-poor but CaO-rich parent melt.

As most chondrules are low in Na and have much lower CaO contents than 20 wt%, we conclude that RF found in chondrules has not crystallized in situ but that these RF are xenocrysts that were accidentally captured by the chondrule melt. Textural and mineral chemical arguments exist to support this view. The zoning of CaO and $Al_2O_3$ in RF (Fig. 15) is always opposite to what is expected from olivine crystallizing in a closed system (Figs. 16a and 16b). In Figs. 16c and 16d, a zoning pattern of a "normal" chondrule olivine from Chainpur (LL3.4) is displayed. Concentrations of CaO are very low (0.08 wt%) in the core and increase toward the rim due to enrichment of CaO in the residual melt. The increase in CaO is accompanied by a parallel but less steep increase in FeO and MnO, reflecting normal igneous zoning. The decrease in CaO at the outermost rim of the chondrule is the result of low temperature equilibration.

Refractory forsterites have a very different CaO zoning, with constant CaO in the central area of the grain and decreasing CaO toward the rim. Some forsterites have a convex shaped CaO pattern with a maximum in the center and continuously decreasing CaO and $Al_2O_3$ toward the rim (Fig. 18a). This "reversed zoning" is opposite to what one would expect from closed system crystallization. It requires decreasing CaO and $Al_2O_3$ contents of the melt during olivine crystallization (Figs. 16b and Fig. 18a). The decrease of Al torward the rims of RFs could also reflect the decrease of the Al olivine/melt partition coefficients with temperature (Agee and Walker 1990), but this explanation is not applicable to Ca, as the CaO partition coefficient is independent of temperature (see Libourel 1999). To explain this CaO pattern and also the more common CaO patterns of RF with constant CaO in the interior and some decrease at the rim, Pack et al. (Forthcoming) suggested that RF crystallized from melts that are primary condensates from a gas. During cooling, melt condensates become increasingly less refractory by condensation of Mg and Si (Fig. 17). The continuous change in melt composition is recorded in the decreasing Ca and Al

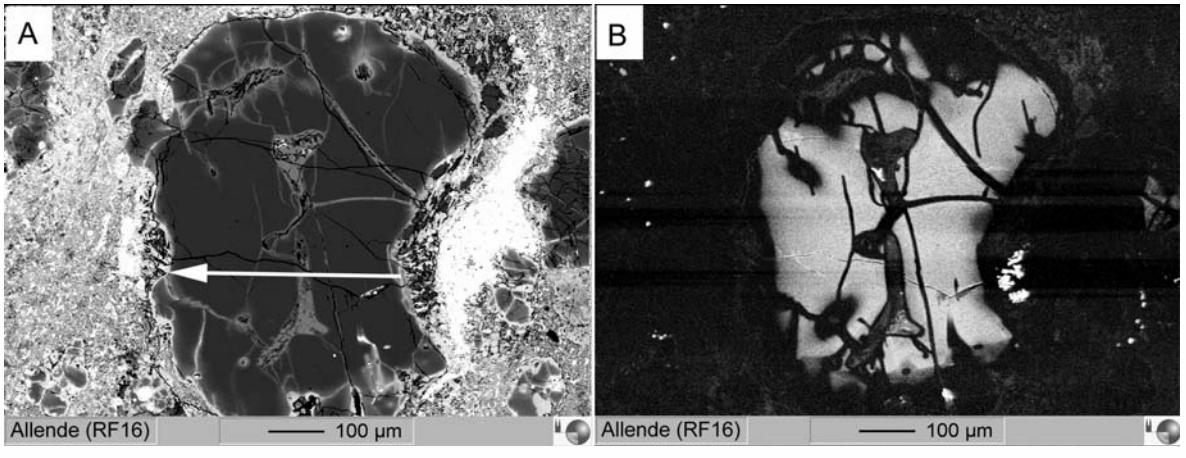


Fig. 15. Isolated refractory forsterite from Allende (CV3): a) BSE image with the position of the chemical profile indicated; b) CL image showing the bright luminescent core.

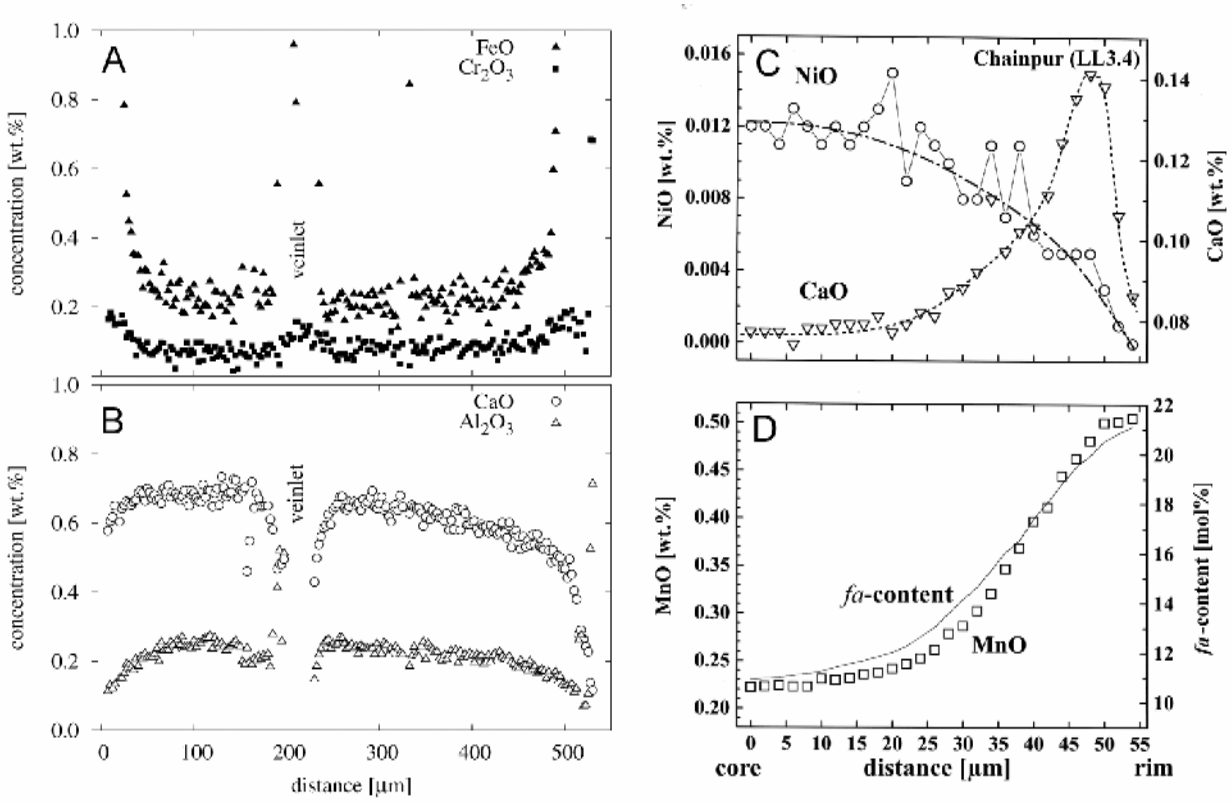


Fig. 16. EPMA profiles across (a, b) isolated RF (RF16, see Fig. 15) and (c, d) a "normal" zoned chondritic olivine from Chainpur (LL3.4, modified after Petry [1998], personal communication). Note the low CaO concentrations in the "normal" olivine grain compared to RF16. The decrease in CaO toward the outermost rim points to diffusive CaO loss at low temperatures.

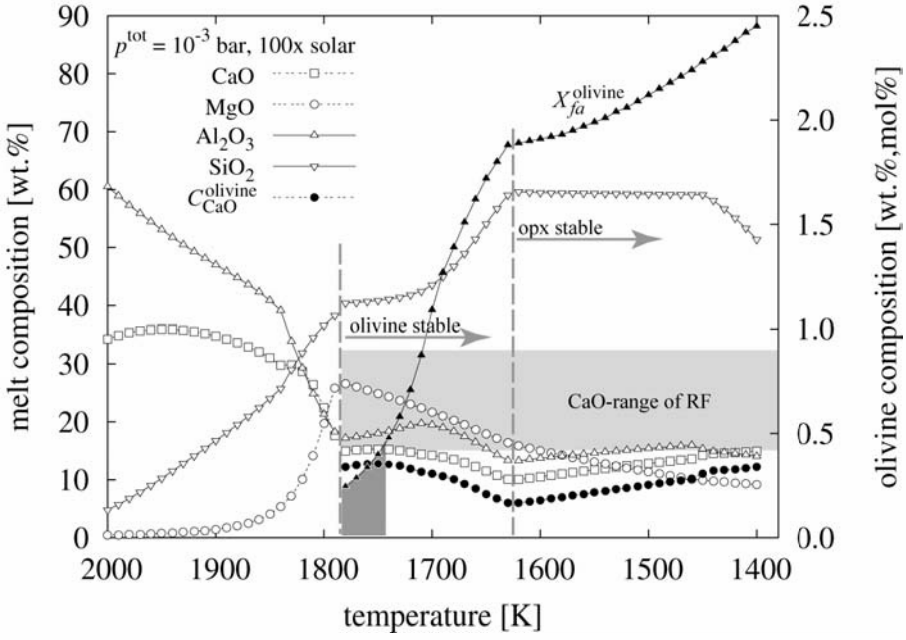


Fig. 17. Plot of the composition of melt condensates versus the temperature (data from Ebel and Grossman [2000]). The olivine composition (fa, CaO) can be read from the right ordinate. The light gray shaded area outlines the compositional range (CaO content) of RF. The dark gray shaded area outlines the typical FeO contents (0.25–0.5 mol% fa) of RF.

contents of the crystallizing forsterites. This "open system fractional crystallization" model (OSFC) is capable of explaining the observed zoning of Ca and Al in forsterite.

Yoneda and Grossman (1995) and Ebel and Grossman (2000) demonstrated that liquids can condense from a nebula at enhanced dust/gas ratios and/or at enhanced total pressures. At low dust/gas ratios, these melt condensates are FeO-poor and refractory lithophile element-rich (Fig. 17). Since these melt condensates are free of alkalis, which condense at much lower temperatures, our experiments, along with the equilibrium CMAS and CMAS-Ti data by Libourel (1999), are applicable to the Ca partitioning between melt condensate and forsteritic olivine.

In the OSFC model, RF is crystallizing within a refractory melt condensate during ongoing condensation, i.e., open system fractional crystallization. The decrease in CaO and the increase in FeO toward the rims of RF grains (see Figs. 16a and 16b) are explained by a continuous compositional change of the melt during condensation of the major melt components $SiO_2$, MgO, and some FeO. As a result of the changing melt composition, the forsterites become less refractory and more ferrous toward their rims. Hence, the zoning of RF (Figs. 16a and 16b; Fig. 18a) reflects the condensation sequence, where refractory lithophile elements (Ca, Al) condense at higher temperatures (i.e., earlier) than common lithophile (Si, Mg) and oxidizable lithophile elements, respectively. In this respect, zoned RFs may be compared to zoned metal grains as described by Meibom et al. (1999, 2001). These metal grains are a few hundred microns across and consist of a Ni-rich core and a Ni-poor rim (Fig. 18b). The Ni content gradually decreases toward the rim. Meibom et al. (2001) and Petaev et al. (2001) inferred from the zoning that the cores condensed at about 1500 K and the "less refractory" rims condensed at about 1400 K. Because of the lower diffusion rate of Ca in olivine, the timescale for the preservation of CaO zoning is larger than that of Ni zoning in metal grains.

Ebel and Grossman (2000) calculated the compositional variation of melts during equilibrium condensation. The first melt condensates are very rich in CaO and $Al_2O_3$ and poor in FeO. With proceeding condensation of $SiO_2$ and MgO, the melt becomes less refractory. At a total pressure of $10^{-3}$ bar and a dust/gas ratio of 100 × solar, forsterite saturation of the liquid is reached at 1790 K (Fig. 17). According to Ebel and Grossman (2000), the first forsterite in equilibrium with the melt condensate should contain 0.25 wt% FeO and 0.73 wt% CaO ($p = 10^{-3}$ bar, 100 × solar dust/gas). This value, however, is in disagreement with our and Libourel's (1999) Ca partitioning data, which predict a CaO content of 0.34 wt% (see also Pack et al. [Forthcoming]). With decreasing temperature, the CaO content of the liquid decreases, while the FeO content increases rapidly (Fig. 17). With proceeding condensation, CaO decreases in the melt, while $Al_2O_3$ increases in the interval between 1790 and ≈1700 K (Fig. 17). The increase in $Al_2O_3$ is related to spinel dissolution in that temperature range. The continuous decrease in $Al_2O_3$ from the core to the rim of RF may be the result of decreasing $D_{Al}^{ol/melt}$ with decreasing temperature.

According to Ebel and Grossman (2000), a dust/gas enrichment of 100 × solar is sufficiently oxidizing to stabilize an olivine with ~2 mol% fayalite at the pyroxene appearance temperature (Fig. 17). RF contains typically <1 mol% fayalite. Based on this fact, the oxygen isotope composition, and on the CaO contents of RF, which exceed 0.34 wt% (Fig. 17), Pack et al. (Forthcoming) suggested that RF formed in an environment with an initial (i.e., before evaporation) dust/gas ratio in the range of 7–8 × solar.

In the OSFC model by Pack et al. (Forthcoming), RF was assumed to have crystallized within melt condensates. This

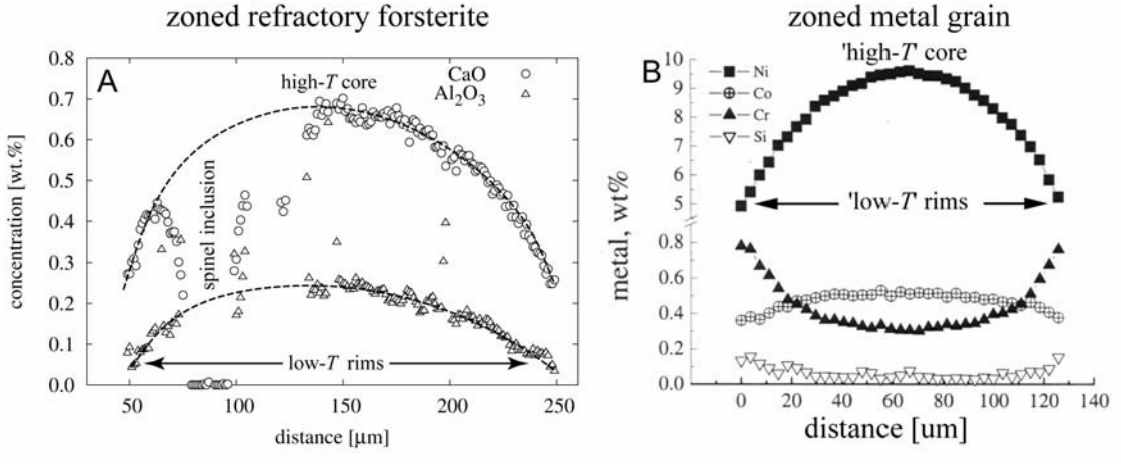


Fig. 18. a) Plot of CaO and $Al_2O_3$ across a zoned forsterite grain from Vigarano (CV3, modified after Pack et al. [Forthcoming]). CaO and $Al_2O_3$ are high in the core and decrease toward the rims. The profile is disturbed by a crack and a spinel inclusion; b) plot of the Ni, Co, Cr, and Si content of a zoned metal grain from CH chondrite PAT 91546 (modified after Meibom et al. [1999], Fig. 2 therein).

assumption was primarily based textural arguments. The size of RF grains as well as the occurrence of melt inclusion within these forsterites was used to argue against a condensation origin of RF (e.g., Weinbruch et al. 2000). Furthermore, a textural, a chemical, and an O-isotope continuum appears to occur between the isolated RF grains and weakly luminescent forsterites from porphyritic type-IA chondrules (see Pack et al. Forthcoming). In light of condensed metal grains with a diameter of a few hundred microns (Meibom et al. 1999, 2001), condensation of large forsterite grains may also be possible. Furthermore, stabilizing melt condensates at a dust/gas ratio of 7–8 × solar and $p^{tot} = 10^{-3}$ bar, to condense the parent melt for refractory forsterites, is difficult. In conclusion, at present, we cannot exclude any of the 2 possible options for the formation of RF; both crystallization from a CaO-rich melt and condensation from a gas of solar composition appear possible.

Since forsterite is the first major phase to condense from the solar nebula, the low modal content of RF within unequilibrated chondrites (≤0.3 vol%; Pack and Palme 2001; Pack et al. Forthcoming) seems surprising. One possibility is that only a small fraction of forsterite condensed to larger grains and, therefore, could survive nebular and parent body alteration. Our hypothesis is that only those forsterites, which crystallized within melt condensates, could grow to sizes of a few hundred microns, while the majority of Si and Mg condensed into fine-grained forsterite. In contrast to the fine-grained forsterites, only those which could grow within melt condensates could reach an appreciable size and survive nebula and parent body alteration.

*Acknowledgments*–R. Schumacher (Bonn) is thanked for loaning thin sections of Vigarano (CV3). This work was supported by the Deutsche Forschungsgemeinschaft (DFG-grant PA 346/24–1). Furthermore, we appreciate helpful discussions with M. Klein (Cologne) concerning the experimental work. C. B. Agee and J. Longhi are thanked for their reviews.

*Editorial Handling*—Dr. Randy Korotev

## REFERENCES

Agee C. B. and Walker D. 1990. Aluminum partitioning between olivine and ultrabasic silicate liquid to 6 GPa. *Contributions to Mineralogy and Petrology* 105:243–254.

Beattie P. 1994. Systematics and energies of trace element partitioning between olivine and silicate melts: Implications for the nature of mineral/melt partitioning. *Chemical Geology* 117: 57–71.

Blum K. 1982. Instrumentelle Neutronenaktivierung zum Studium der Elementverteilung in den Mineralphasen von Mantelgesteinen. PhD thesis, Johannes Gutenberg-Universität, Mainz, Germany. 174 p.

Brice J. C. 1965. *The growth of crystals from the melt.* Amsterdam: North Holland Publishing Company. 192 p.

Cohen B. A., Hewins R. H., and Yu Y. 2000. Evaporation in the young solar nebula as the origin of "just-right" melting of chondrules. *Nature* 406:600–602.

Colson R. O., McKay G. A., and Taylor L. A. 1988. Temperature and composition dependencies of trace element partitioning: Olivine/melt and low-Ca pyroxene/melt. *Geochimica et Cosmochimica Acta* 52:539–553.

Conolly H. C., Jones B. D., and Hewins R. H. 1998. The flash melting of chondrules: An experimental investigation into the melting history and physical nature of chondrule precursors. *Geochimica et Cosmochimica Acta* 62:2725–2735.

Donaldson C. H. 1976. An experimental investigation of olivine morphology. *Contributions to Mineralogy and Petrology* 57: 187–213.

Ebel D. and Grossman L. 2000. Condensation in dust-enriched systems. *Geochimica et Cosmochimica Acta* 64:339–366.

Gooding J. L., Mayeda T. K., Clayton R. N., Fukuoka T. 1983. Oxygen isotope heterogeneities, their petrological correlations, and implications for melt origins of chondrules in unequilibrated chondrites. *Earth and Planetary Science Letters* 63:209–224.

Hewins R. H. 1997. Chondrules. *Annual Review of Earth and Planetary Sciences* 25:61–83.

Hervig R. L. and Steele I. M. 1992. Oxygen isotope analysis of Allende olivine by ion probe and implications for chondrule origin (abstract). 23rd Lunar and Planetary Science Conference. pp. 525–526.

Jones R. H. 1992. On the relationship between isolated and chondrule olivine grains in carbonaceous chondrite ALH A77307. *Geochimica et Cosmochimica Acta* 56:467–482.

Jones R. H. 1996. Relict grains in chondrules: Evidence for chondrule recycling. In *Chondrules and the protoplanetary disk,* edited by Hewins R. H., Jones R. H., and Scott E. R. D. Cambridge: Cambridge University Press. pp. 163–172.

Jones R. H., Saxton I. M., Lyon I. C., and Turner G. 2000. Oxygen isotopes in chondrule olivine and isolated olivine grains from the CO3 chondrite Allan Hills A77307. *Meteoritics & Planetary Science* 35:849–857.

Kennedy A. K., Lofgren G. E., and Wasserburg G. J. 1993. An experimental study of trace element partitioning between olivine, orthopyroxene, and melt in chondrules: Equilibrium values and kinetic effects. *Earth and Planetary Science Letters* 115:177–195.

Klerner S., Jones R. H., Palme H., and Shearer C. K. 2000. Trace elements and cathodoluminescence in refractory forsterite from Allende and Kaba (abstract #1689). 31st Lunar and Planetary Science Conference.

Klerner S. 2001. Materie im frühen Sonnensystem: Die Entstehung von Matrix, Chondren und refraktärem Forsterit. PhD thesis, Universität zu Köln, Köln, Germany. 119 p.

Köhler T. P. and Brey G. P. 1990. Calcium exchange between olivine and clinopyroxene calibrated as geothermometer for natural peridotites from 2 to 60 kb with applications. *Geochimica et Cosmochimica Acta* 54:2357–2388.

Libourel G. 1999. Systematics of calcium partitioning between olivine and silicate melt: Implications for melt structure and calcium content of magmatic systems. *Contributions to Mineralogy and Petrology* 136:63–80.

Lofgren G. E. 1996. Dynamic crystallization model for chondrule melts. In *Chondrules and the protoplanetary disk,* edited by Hewins R. H., Jones R. H., and Scott E. R. D. Cambridge: Cambridge University Press. pp. 187–196.

McSween H. Y., Jr. 1977. On the nature and origin of isolated olivine grains in carbonaceous chondrites. *Geochimica et Cosmochimica Acta* 41:411–418.

Meibom A., Petaev M. I., Krot A. N., Wood J. A., and Keil K. 1999.

Primitive FeNi metal grains in CH carbonaceous chondrites formed by condensation from a gas of solar composition. *Journal of Geophysical Researc*h 104:22053–22059.

Meibom A., Petaev M. I., Krot A. N., Keil K., and Wood J. A. 2001. Growth mechanism and additional constraints on FeNi metal condensation in the solar nebula. *Journal of Geophysical Research* 106:32797–32801.

Osborn E. F., Devries R. C., Gee K. H., and Kraner H. M. 1954. Optimum composition of blast-furnace slags as deduced from liquidus data for the ternary system CaO-MgO-$Al_2O_3$-$SiO_2$. *Transactions of the American Institute of Mining and Metallurgical Engineers* 200:33–45.

Pack A. and Palme H. 2001. Distribution and characteristics of refractory forsterite in ordinary and carbonaceous chondrites (abstract). *Meteoritcs & Planetary Science* 36:A156.

Pack A., Sauerborn M., Klerner S., Palme H., Neumann A., and Seboldt W. 2002a. Dynamic crystallization experiments using conventional and solar furnace techniques-Implications for the formation of refractory forsterite in chondrites (abstract). European Geophysical Society, 27th General Assembly #EGS02–A–01829–4.

Pack A., Huth J., and Palme H. 2002b. Cathodoluminescence spectra of refractory forsterites from carbonaceous chondrites (abstract). *Meteoritics & Planetary Science* 37:A114.

Pack A. and Palme H. 2002c. Partitioning of refractory lithophile elements between olivine and silicate melt-influence of the cooling rate (abstract). *European Journal of Mineralogy* 14: 123.

Pack A., Yurimoto H., and Palme H. Forthcoming. Petrographic and oxygen isotope study of refractory forsterites from R chondrite Dar al Gani 013 (R3–6), unequilibrated ordinary and carbonaceous chondrites. *Geochimica et Cosmochimica Acta.*

Palme H. and Fegley B., Jr. 1990. High-temperature condensation of iron-rich olivine in the solar nebula. *Earth and Planetary Science Letters* 101:180–195.

Petaev M. I., Meibom A., Krot A. N., Wood J. A., and Keil K. 2001. The condensation origin of zoned metal grains in QUE 94411: Implications for the formation of the Bencubbin-like chondrites. *Meteoritics & Planetary Science* 36:93–106.

Roedder E. 1981. Significance of Ca-Al-rich silicate melt inclusions in olivine crystals from the Murchison type II carbonaceous chondrite. *Bulletin de Minéralogie* 104:339–353.

Rubin A. E. and Wasson J. T. 1987. Chondrules, matrix and coarse-grained chondrule rims in the Allende meteorite: Origin, interrelationship, and possible precursor components. *Geochimica et Cosmochimica Acta* 51:1923–1937.

Sears D. W., Lyon I., Saxton J., and Turner G. 1998. The oxygen isotope properties of olivines in the Semarkona ordinary chondrite. *Meteoritics & Planetary Science* 33:1029–1032.

Steele I. M., Smith J. V., and Sirikus C. 1985. Cathodoluminescence zoning and minor elements in forsterites from the Murchison (C2) and Allende (C3V) carbonaceous chondrites. *Nature* 313: 294–297.

Steele I. M. 1986. Cathodoluminescence and minor elements in forsterites from extraterrestial samples. *American Mineralogist* 71:966–970.

Weinbruch S., Zinner E., El Goresy A., Steele I. M., and Palme H. 1993. Oxygen isotopic composition of individual olivine grains from the Allende meteorite. *Geochimica et Cosmochimica Acta* 57:2649–2661.

Weinbruch S., Palme H., and Spettel B. 2000. Refractory forsterite in primitive meteorites: Condensates from the solar nebula? *Meteoritics & Planetary Science* 35:161–171.

Yoneda S. and Grossman L. 1995. Condensation of CaO-MgO-$Al_2O_3$-$SiO_2$ liquids from cosmic gases. *Geochimica et Cosmochimica Acta* 59:3413–3444.